

Enhancing Electronic and Optical Properties of α -Fe₂O₃ by Introducing B, Y, and Nb Dopants for Improved Photoelectrochemical Water Splitting

Abdul Ahad Mamun¹ and Muhammad Anisuzzaman Talukder^{1,*}

¹Department of Electrical and Electronic Engineering,
Bangladesh University of Engineering and Technology,
Dhaka 1205, Bangladesh,
**anis@eee.buet.ac.bd*

Abstract

Advanced theoretical investigations are crucial for understanding the structural growth mechanisms, optoelectronic properties, and photocatalytic activity of photoelectrodes for efficient photoelectrochemical water splitting. In this work, we conducted first-principles calculations aimed at designing α -Fe₂O₃ photoelectrodes incorporating mono-dopants such as boron (B), yttrium (Y), and niobium (Nb), as well as co-dopants (B, Y) and (B, Nb) to enhance the performance of photoelectrochemical cells (PECs). We assessed the thermodynamic phase stability by calculating formation enthalpy (E_f) and examining material properties, including microstrain (μ_ϵ) and crystallite size (D). The mono-dopants, Y and Nb, and the co-dopants, (B, Y) and (B, Nb), exhibited negative E_f values under the substitutional doping method, confirming their thermodynamic phase stability and suggesting their practical viability for experimental implementation. Notably, the values of μ_ϵ and D fell within the ranges observed experimentally for α -Fe₂O₃, indicating their effectiveness in growth mechanisms. To gain a comprehensive understanding of the optoelectronic properties of doped α -Fe₂O₃, we calculated the electronic band structure, density of states, atom's ionic charge, and optical absorption coefficient (α). This analysis allowed us to examine the improvements in the electronic charge characteristics and photon-electron interactions. B-doped α -Fe₂O₃ led to the formation of impurity bands, which were effectively mitigated by utilizing co-dopants (B, Y) and (B, Nb). The metal dopants, Y and Nb, significantly increased the charge carrier density, while the co-dopants, (B, Y) and (B, Nb), substantially enhanced light absorption in the visible spectrum.

These improvements in the electronic and optical properties of α -Fe₂O₃ indicate its potential for application in photocatalytic water splitting.

1 Introduction

Converting solar energy into renewable hydrogen (H₂) fuel through water (H₂O) splitting reactions in photoelectrochemical cells (PECs) is considered a promising third-generation energy conversion technology [1, 2]. It generates zero carbon emissions and presents a favorable alternative to fossil fuels by enabling sustainable and efficient PEC performance [1, 3]. The U.S. Department of Energy has established standard performance targets for PEC systems, requiring $\sim 10\%$ solar-to-hydrogen efficiency (η_{STH}) and ~ 1000 hours of durability, both of which critically depend on the photoelectrode [4, 5]. Semiconductor materials serve as photoelectrodes by absorbing sunlight to generate electron-hole pairs, resulting in photoinduced current density (J_{ph}) and potential (V) [1, 6]. In PECs, the produced (V) must exceed the combined values of the standard water-splitting redox potential (E_{rx}^0) and the losses associated with the PEC system to facilitate charge carrier transfer at the interfaces between the photoelectrode and the electrolyte for oxygen (OER) and hydrogen evolution reactions (HER) [7, 8]. To meet the requirements of the PEC system, the photoelectrode should have a bandgap energy (E_g) in the range of 1.6 to 2.0 eV and achieve a minimum J_{ph} of 8.2 mAcm⁻² [9, 10]. Furthermore, enhancing the kinetic rate of evolution reactions and ensuring the electrochemical stability of the photoelectrode are crucial for efficient H₂ production and longevity [11, 12]. These advancements are key to unlocking the full potential of solar H₂ as a clean and renewable energy source for the future.

In recent decades, extensive research has explored various semiconductors as photoelectrodes, including compound semiconductors (CSs), transition metal oxides (TMOs), transition metal carbides (TMCs), metal nitrides (MNs), metal selenides (MSs), and metal chalcogenides (MCs) [6, 13–17]. Among these, TMOs—chemical compounds comprising various transition metals and oxygen—represent a promising class of materials to use as photoelectrodes for advancing PEC systems due to technically and economically feasible synthesis processes [18, 19]. TMOs offer several advantages, including the presence of oxygen vacancy defect sites, tunable E_g , and diverse morphological structures [20]. Additionally, they are low-cost, abundant in nature, and demonstrate exceptional photochemical stability in electrolytes under sunlight [21].

Despite these advantages, the widespread application of TMOs in PEC systems faces significant challenges. They inherently form polarons and comprise charge carrier quasi-particles, resulting in inefficient electron-hole pair separations [22]. Specifically, TMOs have a larger E_g , limiting their ability to absorb a significant portion of solar irradiance, leading to insufficient charge carrier generation and J_{ph} [22, 23]. Furthermore, rapid charge carrier recombination within the

bulk material and slower charge transfer kinetics at the interface between TMOs and electrolytes present critical barriers to large-scale H₂ production via photoelectrochemical water splitting [24]. Recently, researchers have focused on developing new methods and approaches to enhance the optoelectronic properties and photocatalytic activity of various TMOs, such as α -Fe₂O₃, TiO₂, BiVO₄, WO₃, CuO, and CdWO₄. [25–27].

α -Fe₂O₃, commonly known as hematite, is regarded as one of the most effective photoelectrodes for PEC applications due to several key factors: the favorable oxidized states of Fe atom (Fe²⁺ and Fe³⁺), its substantial abundance in the Earth’s crust, non-toxicity, and high electrochemical stability across a wide range of pH levels in electrolytes [4, 28]. Notably, the band edge position relative to the redox potential of water oxidation, along with a relatively suitable E_g of \sim 2.2 eV, makes α -Fe₂O₃ a preferred material for photoanodes, enabling it to ideally utilize \sim 40% of solar energy for photoabsorption [29]. If all photons with energy $>$ 2.2 eV produce electron-hole pairs with 100% quantum yield efficiency, the J_{ph} and power conversion efficiency (η_{PCE}) of α -Fe₂O₃ could theoretically reach \sim 12.6 mAcm⁻² and \sim 12.9% in photoelectrochemical water splitting [30]. However, the use of pristine α -Fe₂O₃ in the PEC system is limited due to its poor electrical conductivity ($<$ 1 cm²V⁻¹s⁻¹), a rapid charge carrier recombination rate (\sim 10 ps), a short diffusion length (2–4 nm), and the difficulty of exciting d-orbital electrons with only a small portion of visible light (up to $<$ 564 nm) [31–33]. Additionally, insufficient charge carrier separation and a less favorable surface structure of pristine α -Fe₂O₃ for evolution reactions reduce charge transfer kinetics, leading to overall poor PEC performances [34]. Therefore, it is crucial to address these challenges by employing effective enhancement strategies to fully realize the potential of α -Fe₂O₃ in efficient and sustainable photoelectrochemical water splitting.

Several enhancement strategies, such as structural engineering, surface modification, and doping methods, have been thoroughly studied to address the drawbacks of pristine α -Fe₂O₃ [35–37]. Among these strategies, the doping technique is particularly effective in improving the electronic structure, optical properties, and photocatalytic activity [37]. A variety of mono-dopants, such as N, Sn, Ti, Si, Pt, Zr, Ge, Cr, and Zn, and co-dopants, such as (N, Zn), (N, Ti), and (Pd, Eu, Rb), have been introduced in pristine α -Fe₂O₃ experimentally to improve the PEC performances [38–43]. Nevertheless, due to the extensive efforts and complexity of the experimental processes, it remains challenging to identify the most appropriate dopants and understand the mechanisms that enhance optoelectronic properties and photocatalytic activity. To theoretically address these challenges, the first-principles study is considered an essential approach to examine the design of dopants and assess their effects on electronic structures and optical properties [44]. For instance, mono-dopants, such as Be, N, Al, Si, Ni, Ti, Zr, Ge, Rh, and Sn, have been studied, along with co-doping combinations, such as (N, Zr), (N, Ti), and (Be, Sn), to enhance the optoelectronic properties and photocatalytic activity of pristine α -Fe₂O₃ for photoelectrochemical water splitting [43, 45–48].

The potential for discovering new dopants and co-dopants in pristine α -Fe₂O₃ is substantial, offering exciting opportunities for significantly improving the PEC performances.

To further explore the enhancement of the PEC performances of pristine α -Fe₂O₃, this work aimed at designing a modified α -Fe₂O₃ incorporating mono-dopants, such as boron (B), yttrium (Y), and niobium (Nb), and co-dopants, such as (B, Y) and (B, Nb), using first-principles density functional theory (DFT). Firstly, we investigated the thermodynamic phase stability of doped α -Fe₂O₃ by computing formation enthalpy (E_f) while considering substitutional and interstitial doping methods. The results revealed that the substitutional mono-dopants, Y and Nb, and co-dopants, (B, Y) and (B, Nb), exhibited negative E_f values, suggesting that these dopants are thermodynamically favorable and practically viable for experimental implementation. Secondly, we examined the material characteristics of the modified doped α -Fe₂O₃ by calculating bulk strain (μ_B), microstrain (μ_ϵ), crystallite size (D), and dislocation density (δ) using X-ray diffraction (XRD) patterns and the Williamson-Hall (WH) method. Thirdly, we calculated the electronic band structures, density of states (DOS), and atom ionic charge to analyze the charge carrier localization in the valence band maximum (VBM) and conduction band minimum (CBM), E_g , and charge carrier density. The doped α -Fe₂O₃ exhibited a reduced E_g , improved charge carrier delocalization, and increased atom ionic charge, demonstrating enhanced free charge carrier density and electrical conductivity. Finally, we determined the optical absorption coefficient (α) incorporating the real and imaginary parts of permittivity for both pristine and doped α -Fe₂O₃. The dopants B, (B, Y), and (B, Nb) into α -Fe₂O₃ displayed significant red-shifted light absorption in the visible spectrum. Our results reveal that the proposed dopants and doping methods could substantially enhance the photocatalytic activity of α -Fe₂O₃, making it a promising non-toxic, low-cost, earth-abundant, and durable photoelectrode for efficient photoelectrochemical water splitting.

2 Computational Methodology

This work performed all calculations within the framework of spin-polarized DFT using the self-consistent ab initio method implemented in the Quantum Espresso (QE) code [49]. The exchange-correlation functions were calculated using the general gradient approximation (GGA) and the Perdew-Burke-Ernzerhof (PBE) model [49, 50]. The projected augmented wave (PAW) methodology was applied to describe the core electrons, while the valence electrons were defined using Kohn-Sham (KS) single-electron orbitals, which were solved by expanding in a plane-wave basis with a cut-off kinetic energy of 60 Ry [51]. Marzari-Vanderbilt smearing was used with a value of 0.01 Ry to aid convergence. The Brillouin-zone integration was carried out using the general Monkhorst-Pack grids of $11 \times 11 \times 1$, and the DFT-D3 method was employed for Van der Waals force corrections [52]. To accurately estimate the self-interacting exchange-correlation functions

in the d-orbitals of transition metal atoms, the PBE+U framework developed by Dudarev et al. was utilized in this simulation [53]. The effective Hubbard correction term, U_{eff} , was set to 4.30, as determined symmetrically by Mosey et al. [54]. The optimized lattice parameters and fully relaxed atomic positions of both pristine and doped $\alpha\text{-Fe}_2\text{O}_3$ were achieved through variable-cell relaxation calculations using the Broyden-Fletcher-Goldfarb-Shanno (BFGS) algorithm until reaching the atom-acting force convergence of $10^{-3} \text{ eV}\text{\AA}^{-1}$ and the energy convergence of 10^{-6} eV .

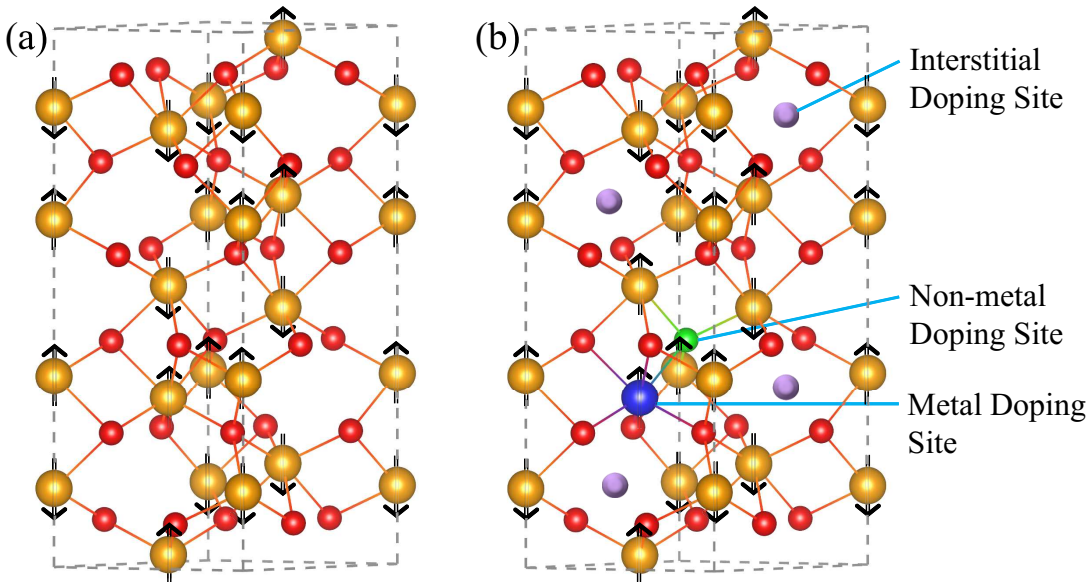


Figure 1: (a) Hexagonal close-packed crystal structure of pristine $\alpha\text{-Fe}_2\text{O}_3$ with the arrow symbol for Fe atom magnetic spin direction at z -axis ([0001] plane). The golden and red spheres represent Fe and O atoms, respectively. (b) The substitutional and interstitial doping sites into $\alpha\text{-Fe}_2\text{O}_3$ for non-metal (N) and metal (M) dopants. The green, blue, and violet spheres indicate non-metal, metal, and interstitial doping sites, respectively.

Figure 1(a) shows the hexagonal close-packed crystal structure of pristine $\alpha\text{-Fe}_2\text{O}_3$ (a space group of $R\bar{3}2/C$), consisting of 12 Fe and 18 O atoms. We chose this crystal structure to create doping models for this work. The bulk $\alpha\text{-Fe}_2\text{O}_3$ exhibits intriguing weak ferromagnetic properties above the Morin transition temperature at $\sim 263 \text{ K}$ and below the Néel temperature at $\sim 955 \text{ K}$ [55, 56]. When the temperature exceeds the Néel point, it transitions to a paramagnetic state. However, below the Morin temperature, it possesses a stable antiferromagnetic ground state, characterized by the magnetic spin orientations of the Fe atoms lying in the [0001] plane, as illustrated in Fig. 1(a) [56, 57]. Substitutional and interstitial doping methods were employed for doping models, as illustrated in Fig. 1(b). In the substitutional method, the positions of the up and down spin Fe atoms were considered doping sites for the metals Y and Nb. In addition, non-metal B replaced the positions of O atoms as substitutional doping sites. The unoccupied spaces within the $\alpha\text{-Fe}_2\text{O}_3$

crystal structure were designated interstitial doping sites for all dopants, including B, Y, and Nb. To model co-dopants into α -Fe₂O₃, Fe and O atoms were substituted by the metal and non-metal dopants, respectively.

To investigate the growth mechanism and assess the relative phase stability of doped α -Fe₂O₃, we calculated the impurity E_f for substitutional mono-dopants and co-dopants using the following equations [58]

$$E_{f,N}^{\text{sub}} = E_N - E_P - \mu_N + \mu_O, \quad (1a)$$

$$E_{f,M}^{\text{sub}} = E_M - E_P - \mu_M + \mu_{\text{Fe}}, \quad (1b)$$

$$E_{f,(N,M)}^{\text{sub}} = E_{(N,M)} - E_P - \mu_N + \mu_O - \mu_M + \mu_{\text{Fe}}. \quad (1c)$$

The impurity E_f for interstitial dopants was determined as

$$E_{f,N/M}^{\text{int}} = E_{N/M} - E_P - \mu_{N/M}, \quad (2)$$

where $E_{f,N}^{\text{sub}}$, $E_{f,M}^{\text{sub}}$, and $E_{f,(N,M)}^{\text{sub}}$ refer to the formation enthalpies of dopants for the substitutional method. Specifically, $E_{f,N}^{\text{sub}}$ refer to the formation enthalpy for mono-doping with a non-metal (N), $E_{f,M}^{\text{sub}}$ for mono-doping with a metal (M), and $E_{f,(N,M)}^{\text{sub}}$ for co-doping with both a non-metal and a metal (N, M). Additionally, $E_{f,N/M}^{\text{int}}$ represents the formation enthalpy of non-metal/metal (N/M) dopants when using the interstitial method. The total system energies due to doping elements are denoted as follows: E_N for substitute mono-doping with N, E_M for substitute mono-doping with M, and $E_{(N,M)}$ for substitute co-doping with both N and M, and $E_{N/M}$ for interstitial doping with N or M dopant. The parameter E_P represents the total energy of pristine α -Fe₂O₃ unit cell. The chemical potentials for N, M, O, and Fe are represented by μ_N , μ_M , μ_O , and μ_{Fe} , respectively. It is important to note that the μ_O and μ_{Fe} values critically depend on the growth mechanism of α -Fe₂O₃, specifically under O-rich and Fe-rich conditions, causing variations in the impurity E_f [59]. To thoroughly examine these variations, we determined E_f for both conditions by calculating μ_O and μ_{Fe} based on the chemical potential of α -Fe₂O₃ ($\mu_{\text{Fe}_2\text{O}_3}$) using the following equation

$$\mu_{\text{Fe}_2\text{O}_3} = 2\mu_{\text{Fe}} + 3\mu_O. \quad (3)$$

Under the Fe-rich (O-rich) condition, the chemical potential μ_{Fe} (μ_O) is calculated from the energy of a bulk Fe (O) atom, while the corresponding μ_O (μ_{Fe}) is determined using Eq. (3).

We evaluated several material characterization parameters for pristine and doped α -Fe₂O₃, such as μ_B , μ_ε , D , and δ . The value of μ_B was calculated by the ratio between the optimized unit cell volume (V_{cell}) of doped and pristine α -Fe₂O₃. Meanwhile, the X-ray diffraction (XRD) pattern and the Williamson-Hall (WH) method were employed to determine the values of μ_ε and D [60]. To obtain the XRD data for the pristine and doped α -Fe₂O₃, we used Vesta Software considering

conventional $\theta/2\theta$ scan at the wavelength (λ_{XRD}) of 1.506 Å (refer to Figs. S1–S3 for the XRD patterns) [61]. The WH equation is given by [60]

$$\beta_{hkl} \cos(\theta) = \frac{K\lambda_{\text{XRD}}}{D} + 4\mu_e \sin(\theta), \quad (4)$$

where β_{hkl} is the integral breadth of the peak associated with the (hkl) plane in the XRD profiles, θ is the diffraction Bragg angle, and K is the shape control factor that commonly has a value of 0.9. The parameter δ is derived from D using $\delta = 1/D^2$. In order to investigate the interaction of optical photons with electrons in both pristine and doped α -Fe₂O₃, α is calculated from the real $\epsilon_{\text{re}}(\omega)$ and imaginary $\epsilon_{\text{im}}(\omega)$ parts of permittivity using [62]

$$\alpha(\omega) = 2\sqrt{\omega} \left[\frac{\sqrt{\epsilon_{\text{re}}^2(\omega) + \epsilon_{\text{im}}^2(\omega)} - \epsilon_{\text{re}}(\omega)}{2} \right]^{1/2}, \quad (5)$$

where ω is the angular frequency, which can be expressed as $\omega = (2\pi c)/\lambda$. Here, c and λ are the speed of light and optical wavelength, respectively.

Table 1: Optimized structural lattice parameters and magnetic moment (μ_m) of pristine α -Fe₂O₃ and doped α -Fe₂O₃ photoelectrodes.

Photoelectrode Name	Method	$a = b$ (Å)	c (Å)	V_{cell} (Å ³)	μ_m (μB/Fe)
pristine α -Fe ₂ O ₃	PBE	4.780	13.320	263.374	-
pristine α -Fe ₂ O ₃	PBE+U	5.147	13.873	318.365	4.168
B doped α -Fe ₂ O ₃	PBE+U	5.158	13.954	321.508	4.181
Y doped α -Fe ₂ O ₃	PBE+U	5.207	14.021	329.218	4.193
Nb doped α -Fe ₂ O ₃	PBE+U	5.214	13.980	329.139	4.124
(B, Y) doped α -Fe ₂ O ₃	PBE+U	5.205	14.030	329.177	4.191
(B, Nb) doped α -Fe ₂ O ₃	PBE+U	5.210	14.081	331.009	4.190

3 Results and Discussion

The doped α -Fe₂O₃ requires investigation into the phase stability, optoelectronic properties, and photocatalytic activity. Firstly, we calculated the optimized structure to examine cell parameters, magnetic properties, and the favorable thermodynamic phase through the value of E_f . Then, we systematically described the material characterization and electronic structure of pristine and doped α -Fe₂O₃, which aids in understanding the growth mechanism and electronic properties, including E_g , charge carrier density, and conductivity. Finally, we presented evidence of improved photocatalytic activity, demonstrating both qualitative and quantitative aspects of this enhancement.

Table 2: Formation enthalpy (E_f) of doped α -Fe₂O₃ photoelectrodes incorporating B, Y, and Nb dopants for substitutional and interstitial doping methods.

Doping Method	Dopant	E_f (eV)	
	Element	Fe-rich	O-rich
Substitutional	B	3.857	4.611
	Y	-2.657	-3.788
	Nb	-3.368	-4.499
	(B, Y)	-1.527	-1.904
	(B, Nb)	-1.991	-2.369
Interstitial	B	6.642	6.642
	Y	2.899	2.899
	Nb	1.208	1.208

3.1 Optimized Structure and Formation Enthalpy

We performed a thorough analysis to calculate the lattice parameters of pristine α -Fe₂O₃ using PBE and PBE+U methods to ensure the reliability of our computational approach. For the PBE method, the simulated lattice parameters $a = b$ and c for pristine α -Fe₂O₃ were 4.780 Å and 13.320 Å, respectively, whereas the experimental values were $a = b = 5.04$ Å and $c = 13.75$ Å [63, 64]. The results obtained using the PBE method were underestimated compared to the experimental findings due to excluding the d-orbital self-interacting forces of the transition metal atoms. Using the PBE+U method with U_{eff} set to 4.30, as reported by Meng et al., the computational values were $a = b = 5.104$ Å and $c = 13.907$ Å [65]. In our simulations using the PBE+U method, the obtained lattice parameters were $a = b = 5.147$ Å and $c = 13.873$ Å, and the corresponding magnetic moment (μ_m) was 4.168 μ_B/Fe . The experimental and computational values of μ_m in the literature are approximately 4.6–4.9 and 4.2 μ_B/Fe [57, 64, 65]. Our calculated results closely match with those in the literature, confirming the validity of our methodology to proceed further with the modeling of doped α -Fe₂O₃. Table 1 presents all the optimized lattice parameters and μ_m of pristine and doped α -Fe₂O₃. The value of μ_m slightly increased for the doped α -Fe₂O₃, except in the case of Nb dopants, where a thermodynamically stable phase occurs in the down-spin position of the Fe atom. Notably, the higher value of μ_m causes an intense magnetic field based on electron spin polarization and Lorentz force, leading to improved charge carrier separation and reduced non-radiative recombination.

In order to effectively explore the potential of non-metal and transition metal dopants in pristine α -Fe₂O₃, we strategically chose B as the non-metal dopant and Y and Nb as transition metal dopants for single element doping. We also assessed co-doping combinations of (B, Y) and (B,

Nb) to investigate the doping mechanisms involving a trivalent non-metal alongside trivalent and pentavalent transition metal dopants. Table 2 shows E_f for all the mono-dopants and co-dopants utilizing substitutional and interstitial doping methods. For the substitutional doping method, the E_f of B dopant was positive under Fe-rich and O-rich conditions, implying its thermodynamic phase instability. In contrast, the mono-dopants, Y and Nb, and the co-dopants, (B, Y) and (B, Nb), exhibited negative E_f values with larger absolute magnitudes under both conditions, demonstrating significant thermodynamic phase stability and suggesting their experimental implementation highly feasible. On the other hand, the interstitial doping method resulted in positive E_f values for B, Y, and Nb dopants, signifying that this approach is endothermic and pristine α -Fe₂O₃ possesses more stability. Thus, it is clear that the interstitial doping method is not a viable option for incorporating B, Y, and Nb dopants into pristine α -Fe₂O₃, emphasizing the importance of favoring substitutional doping strategy for achieving successful experimental outcomes.

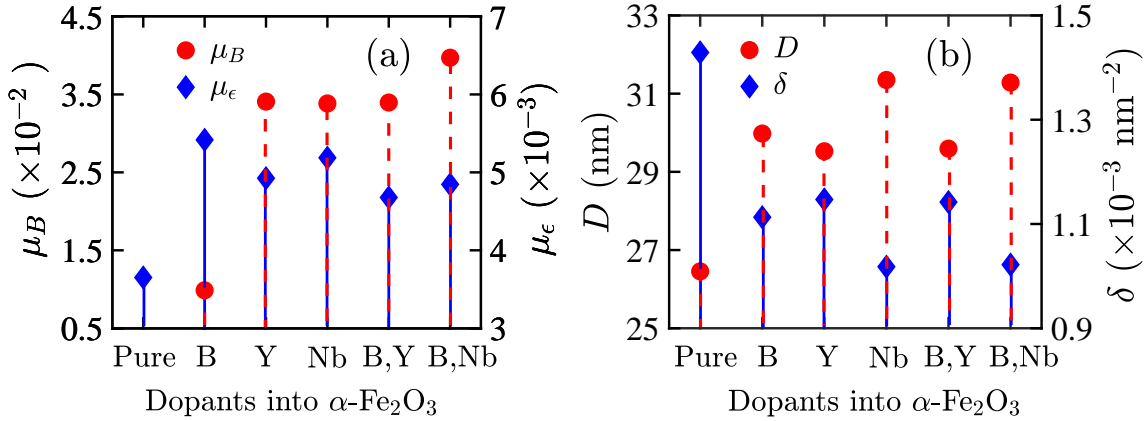


Figure 2: (a) Bulk strain (μ_B) and microstrain (μ_ϵ), (b) crystallite size (D) and dislocation density δ for pristine and doped α -Fe₂O₃ incorporating B, Y, and Nb dopants.

3.2 Material Characterization

The volume of the unit cell in pristine α -Fe₂O₃ can change when dopants are incorporated. The parameter μ_B clearly illustrates the changes in volume associated with expansion or compression of doped α -Fe₂O₃, reflecting how the material responds to bulk stress. A smaller value of μ_B is highly desirable for a photoelectrode, as it signifies a more effective growth mechanism [66]. Notably, B dopant possessed the smallest μ_B value, while co-dopants (B, Nb) had the greatest, as depicted in Fig. 2(a). For the mono-dopants, Y and Nb, and the co-dopants (B, Y), the μ_B value was $\sim 3.4 \times 10^{-2}$. Remarkably, all dopants exhibited $\mu_B < 4\%$, highlighting their potential for practical applications as high-quality α -Fe₂O₃.

The parameter μ_ϵ critically describes the non-uniformity of crystallites and residual lattice

strain in materials across different crystal planes, which can significantly influence the optoelectronic and structural properties. A smaller μ_ϵ indicates better crystallinity with lower lattice deformation and fewer defects, leading to reduced carrier recombination and improved charge transport efficiency [67]. The experimental value of μ_ϵ for pristine α -Fe₂O₃ ranged from 1.51×10^{-3} to 6.2×10^{-3} [68,69]. By utilizing all the crystal plane peak intensities presented in the XRD pattern shown in Fig. S1(a), our calculated average μ_ϵ was 3.65×10^{-3} for pristine α -Fe₂O₃, showing an excellent agreement with the experimental results, as shown in Fig. 2(a). The dopants Y, (B, Y), and (B, Nb) consistently displayed smaller μ_ϵ values, suggesting that they occupy the most favorable sites and serve as more effective dopants. The Nb dopant, although beneficial, showed a comparatively higher μ_ϵ , probably due to its surrounding additional under-coordinated O atoms. On the other hand, the B dopant exhibited the highest μ_ϵ due to excess ligand bonding relative to the O atom, resulting in stronger interactions with Fe atoms that distort the crystalline lattice. Overall, all dopants demonstrated the values of μ_ϵ within the ranges of experimental outcomes for pristine α -Fe₂O₃, indicating their potential effectiveness in structural growth mechanisms and improvements in optoelectronic properties.

The parameter D is critical for measuring the electrical, optical, thermal, magnetic, and chemical properties of the material. A higher value of D leads to increased lattice strain and narrower grain boundary widths, decreasing electrical resistivity and increasing conductivity [70]. Furthermore, the optical properties, such as photoluminescence (PL) intensities and photocatalytic activity, improve with larger D . Similar to microstrain analysis, our calculated average value of D for pristine α -Fe₂O₃ was 26.45 nm, which aligns well with the experimental range of 21 to 32 nm, demonstrating the reliability of our simulations [71]. Figure 2(b) illustrates the values of D for all dopants, with the Nb and (B, Nb) dopants exhibiting the largest D , leading to significantly improved electrical conductivity and photocatalytic activity. For other dopants, the values of D remained higher than pristine α -Fe₂O₃, eventually improving electrical and optical properties. The parameter δ , inversely proportional to the square of D , represents the number of dislocation lines per unit volume within a material that influences various electrical and mechanical properties, including defect sites, charge carrier density, plastic deformation, and tensile strength [72]. In Fig. 2(b), the δ values of all dopants were smaller than pristine α -Fe₂O₃, implying a reduced tensile strength and increased plastic deformation. Nevertheless, the smaller δ resulted in fewer defect sites and larger grain sizes, notably increasing carrier density and decreasing charge transfer resistance (R_{CT}), ultimately enhancing PEC performances.

3.3 Electronic Properties

We examined the electronic band structure and DOS of pristine α -Fe₂O₃ using both the PBE and PBE+U methods. The PBE method underestimated E_g to be 0.24 eV, resulting in inaccuracies in the band structure, as shown in Fig. S4. In contrast, the PBE+U method provided a more accurate estimate of the electronic band structure, reporting an E_g of 2.30 eV, as illustrated in Fig. 3(a). Previous literature has reported an experimental range for E_g between 2.10 eV and 2.40 eV and a calculated value of 2.25 eV, thus assuring the reliability of our approaches and methods [45,65,73,74]. Figure 3(b) presents the DOS of pristine α -Fe₂O₃, highlighting the contributions of the 3d orbitals from Fe and the 2P orbitals from O. The 3d orbitals of Fe atoms primarily contribute to the conduction band (CB), while the valence band (VB) consists of hybridized contributions from the 2p and 3d orbitals of both Fe and O atoms. The near-flatness of the CBM indicates significant localization of charge carriers within the 3d orbitals, leading to a heavy carrier effective mass that complicates electron excitation. Additionally, the relatively large indirect E_g only utilizes a small portion of the solar spectrum, creating substantial challenges for exciting electrons in the 3d orbitals, ultimately leading to very low photoconversion efficiency.

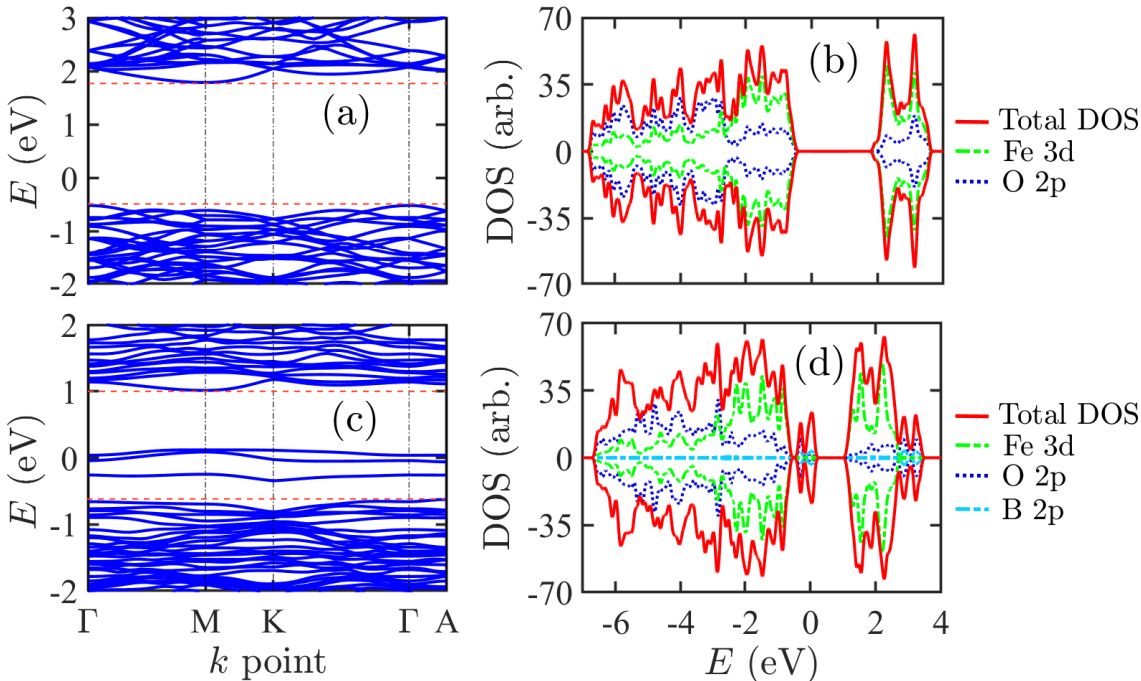


Figure 3: (a) Electronic band structure and (b) density of state (DOS) of pristine α -Fe₂O₃. (c) Electronic band structure and (d) density of state (DOS) of B doped α -Fe₂O₃. For both of them, the Fermi level is set to zero energy.

When the non-metal B dopant replaced the O atom, the E_g reduced to 1.65 eV, significantly

enhancing photoabsorption in the visible spectrum by extending wavelengths up to < 752 nm. In addition, the B dopant introduced acceptor states due to having fewer valence electrons than the O atom, highlighting the potential of B-doped α -Fe₂O₃ as a p-type photoelectrode. However, it is important to note that B doping resulted in several unoccupied impurity bands near the Fermi level, as illustrated in the electronic band structure and DOS in Figs. 3(c) and (d). The VB was composed of a combination of B's 2p, O's 2p, and Fe's 3d orbitals, with the O's 2p orbital playing a dominant role. This dominance caused an upward shift of the VB, making it more efficient at generating holes compared to 3d orbitals. Furthermore, the delocalization of charge carriers in the 3d orbitals was advantageous, as the CBM displayed slightly more curvature than that of pristine α -Fe₂O₃. The smaller E_g allowed for the absorption of more photon energy. The impurity band primarily formed from the interaction between B's 2p orbitals and Fe's 3d orbitals, facilitating the transport of charge carriers through this impurity band at relatively low doping concentrations. However, these impurity bands often acted as recombination defects and trap centers for charge carriers, resulting in lower J_{ph} and poor PEC performance. Therefore, it is essential to address and eliminate these impurity bands, and we aim to overcome these challenges using the co-doping technique.

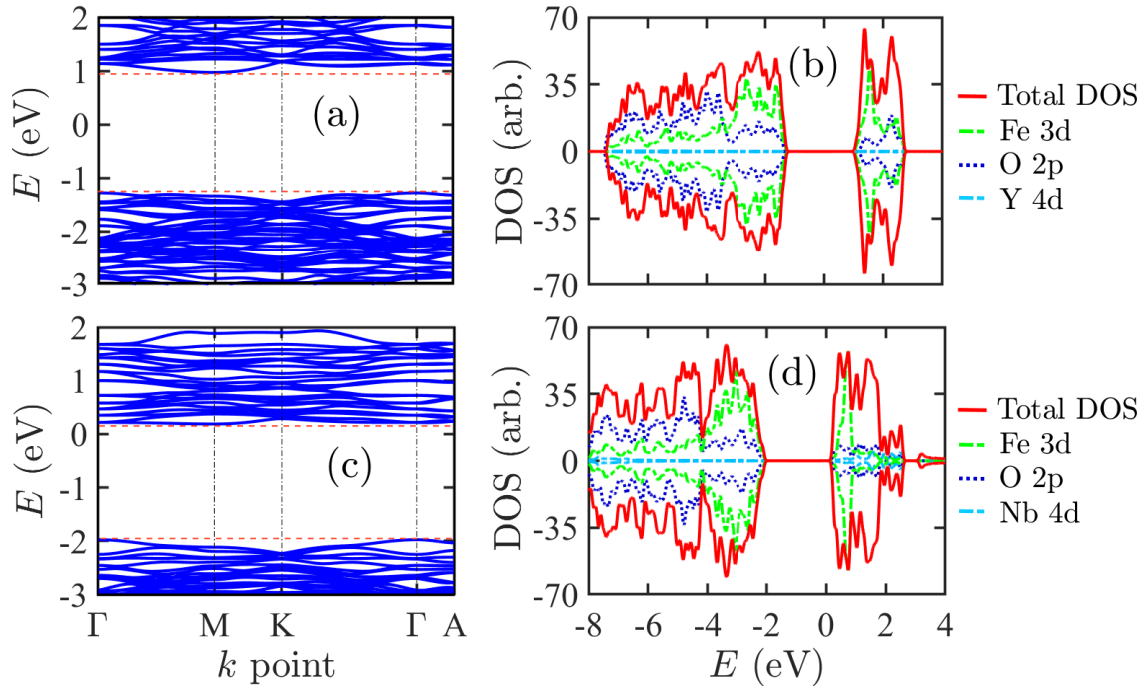


Figure 4: (a) Electronic band structure and (b) density of state (DOS) of Y doped α -Fe₂O₃. (c) Electronic band structure and (d) density of state (DOS) of Nb doped α -Fe₂O₃. For both of them, the Fermi level is set to zero energy.

Next, we investigated the electronic structure of α -Fe₂O₃ doped with Y and Nb, which acted as

donor impurities. Figures 4(a) and (b) present the electronic band structure and DOS for Y-doped α -Fe₂O₃, respectively. The Fermi level was elevated toward the CB, suggesting its potential use as an n-type photoelectrode. The E_g of Y doped α -Fe₂O₃ slightly decreased to 2.25 eV. However, the presence of the Y dopant significantly increased the charge carrier density and delocalization within the CB, primarily by influencing the 4d orbital of the Y atom. This enhancement improves electrical conductivity and the efficiency of charge transport to the photoelectrode surface. In the case of Nb dopant, Figs. 4(c) and (d) depict the electronic band structure and DOS, showing a decrease in E_g by 0.12 eV compared to pristine α -Fe₂O₃. The Fermi level also shifted notably toward the conduction band, further increasing the charge carrier density and reinforcing its role as an n-type photoelectrode. However, the CBM exhibited less curvature than that of pristine α -Fe₂O₃, resulting in a heavier carrier effective mass. This impact adversely affects charge carrier delocalization. Nonetheless, the Nb dopant significantly increased the charge carrier density in the CB, which may help mitigate this adverse effect. Additionally, the VBM with lighter carriers improved charge carrier delocalization, facilitating efficient hole transport toward the photoelectrode surface.

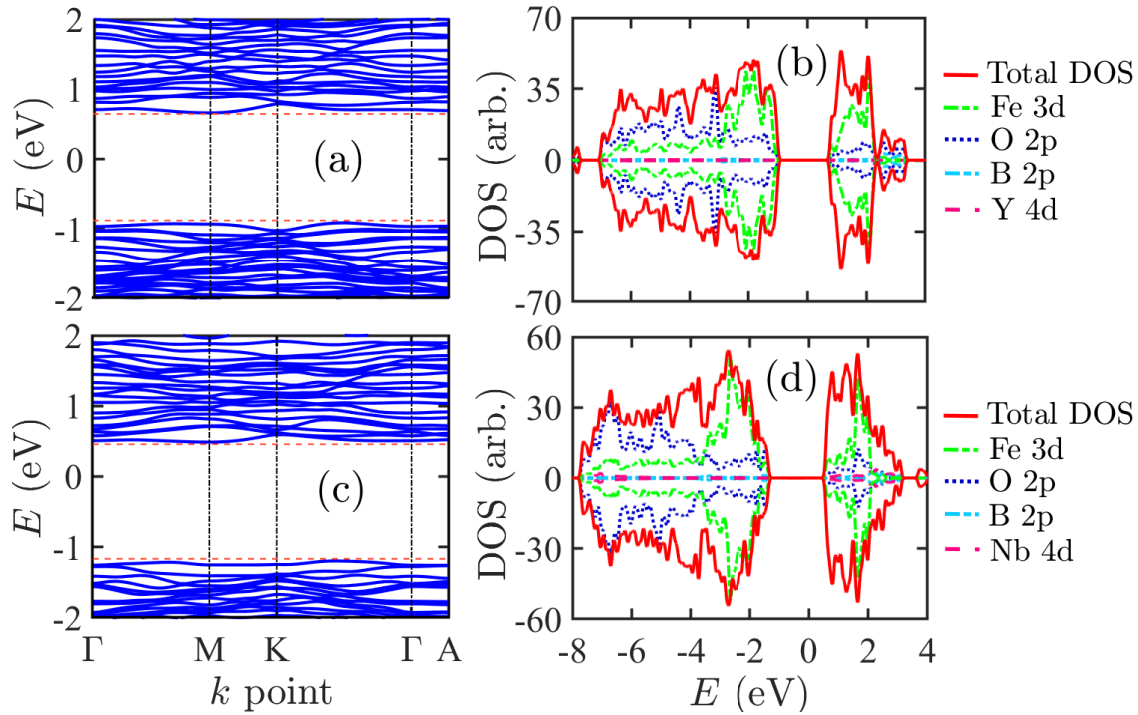


Figure 5: (a) Electronic band structure and (b) density of state (DOS) of (B, Y) co-doped α -Fe₂O₃. (c) Electronic band structure and (d) density of state (DOS) of (B, Nb) co-doped α -Fe₂O₃. For both of them, the Fermi level is set to zero energy.

Based on previous discussions, incorporating both non-metal and metal dopants into pristine

α -Fe₂O₃ exhibited enhanced electronic properties and photocatalytic activity for improved photoelectrochemical water splitting. However, the addition of B as a dopant in α -Fe₂O₃ resulted in the formation of impurity bands, which diminished its effectiveness as a photoelectrode. These challenges can be mitigated by using a combination of n- and p-type impurities as co-dopants. We first investigated the electronic band structure and DOS for (B, Y) co-doped α -Fe₂O₃, as illustrated in Figs. 5(a) and (b). In this scenario, impurity bands did not appear between the CB and the VB, and the corresponding E_g reduced to 1.58 eV. This reduction led to extended photoabsorption capabilities in the visible wavelength spectrum, reaching up to < 785 nm. The donor impurity, Y, played a significant role in (B, Y) co-doped α -Fe₂O₃, indicating its potential as an n-type photoelectrode. The localization of carriers in the CBM and VBM remained similar to that in pristine α -Fe₂O₃, posing challenges for exciting 3d orbital electrons. Nevertheless, the reduced E_g allowed for adequate solar energy absorption, facilitating the excitation of the 3d orbital electrons for efficient transport within the material.

Similarly, (B, Nb) co-doped α -Fe₂O₃ was also considered as an n-type photoelectrode. It did not exhibit any impurity bands in the electronic band structure and DOS, as shown in Figs. 5(c) and (d), respectively. In this case, the E_g was reduced to 1.69 eV, resulting in excellent photoabsorption and enhanced J_{ph} . The CBM of (B, Nb) co-doped α -Fe₂O₃ was more delocalized compared to both the pristine and (B, Y) co-doped α -Fe₂O₃ versions. Furthermore, the Fermi level was positioned closer to the CB, enhancing conductivity and improving the efficiency of charge carrier transport. Overall, introducing (B, Y) and (B, Nb) co-dopants into pristine α -Fe₂O₃ significantly improved its electronic structures and photocatalytic activity, surpassing the effects of mono-doping with B, Y, or Nb alone.

Table 3: Band gap energy (E_g) and electronic charge property of pristine α -Fe₂O₃ and doped α -Fe₂O₃.

Photoelectrode Name	E_g (eV)		Bader Charge (eC)				
	PBE	PBE+U	Fe	O	B	Y	Nb
pristine α -Fe ₂ O ₃	0.24	2.30	+1.822	-1.215	-	-	-
B doped α -Fe ₂ O ₃	0.05	1.65	+1.727	-1.209	-0.181	-	-
Y doped α -Fe ₂ O ₃	0.27	2.25	+1.808	-1.226	-	+2.177	-
Nb doped α -Fe ₂ O ₃	0.14	2.18	+1.748	-1.218	-	-	+2.706
(B, Y) doped α -Fe ₂ O ₃	0.34	1.58	+1.710	-1.224	-0.185	+2.176	-
(B, Nb) doped α -Fe ₂ O ₃	0.26	1.69	+1.658	-1.213	-0.187	-	+2.703

The electronic charge surrounding each atom provides a quantitative measure to understand the ionic charges created by the atoms in the optimized crystal structure. We conducted a Bader charge

analysis on both pristine and doped $\alpha\text{-Fe}_2\text{O}_3$ using the framework of DFT with spin polarization enabled. The calculated average ionic charges for the Fe and O atoms were $+1.822e$ and $-1.215e$, respectively. The B atom exhibited a negative charge of $-0.181e$, indicating that the B dopant acted as an acceptor impurity in B-doped $\alpha\text{-Fe}_2\text{O}_3$. In the case of mono-doping, Y and Nb atoms contributed ionic charges of $+2.177e$ and $+2.706e$, respectively, to $\alpha\text{-Fe}_2\text{O}_3$, resulting in a significant increase in charge carrier density and improved electrical conductivity. Under mono-doping techniques, the ionic charges of Fe slightly decreased, while those of O atoms slightly increased. In contrast, the ionic charge of O in B-doped $\alpha\text{-Fe}_2\text{O}_3$ showed negligible reduction.

Under co-doping conditions, the ionic charges of B, Y, and Nb in $\alpha\text{-Fe}_2\text{O}_3$ were nearly the same as those in the mono-doping scenario. However, the ionic charge of the Fe atom decreased by $+0.112e$ and $+0.164e$ for (B, Y) and (B, Nb) co-doped $\alpha\text{-Fe}_2\text{O}_3$, respectively. This change is influenced by the 2p orbitals of B and the 4d orbitals of the transition metal dopants. Despite this decrease, the significant donor ionic charges from the transition metal dopants greatly enhanced the overall electronic charge properties, leading to enhanced conductivity and J_{ph} in photoelectrochemical water splitting. Table 3 summarizes the electronic charge properties and E_g of both pristine and doped $\alpha\text{-Fe}_2\text{O}_3$ considering the PBE and PBE+U methods. The electronic structures of the doped $\alpha\text{-Fe}_2\text{O}_3$ under the PBE method are presented in the supplementary material (refer to Figs. S4 to S9).

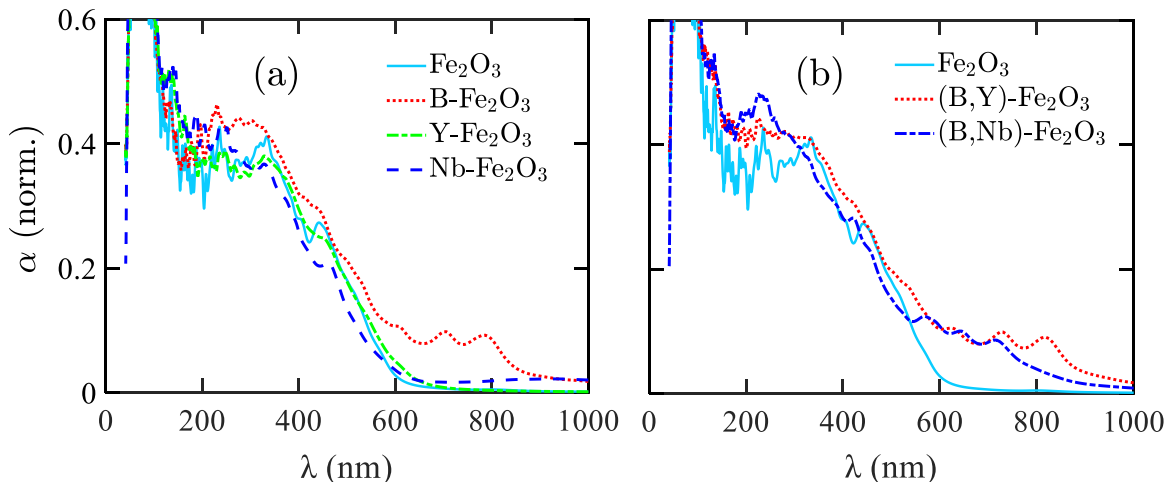


Figure 6: Normalized optical absorption coefficient (α) for (a) pristine $\alpha\text{-Fe}_2\text{O}_3$ and mono-doped $\alpha\text{-Fe}_2\text{O}_3$ and (b) pristine $\alpha\text{-Fe}_2\text{O}_3$ and co-doped $\alpha\text{-Fe}_2\text{O}_3$ photoelectrodes

3.4 Optical Properties

The efficiency of photoabsorption is a crucial factor for photoelectrodes, as it determines how effectively photons interact with electrons in both pristine and doped $\alpha\text{-Fe}_2\text{O}_3$ materials. In our

analysis of photoabsorption, we calculated the normalized absorption coefficient for both pristine and doped $\alpha\text{-Fe}_2\text{O}_3$, as illustrated in Figs. 6(a) and (b). Notably, the normalized absorption coefficient of B-doped $\alpha\text{-Fe}_2\text{O}_3$ exhibited a significant redshift in the visible spectrum, greatly enhancing its performance compared to pristine $\alpha\text{-Fe}_2\text{O}_3$ across the wavelength range of 100 to 800 nm. In contrast, Y-doped $\alpha\text{-Fe}_2\text{O}_3$ showed almost the same absorption characteristics similar to those of pristine $\alpha\text{-Fe}_2\text{O}_3$, while Nb-doped $\alpha\text{-Fe}_2\text{O}_3$ demonstrated improved photoabsorption in the visible spectrum. The most photoactive range for both pristine and mono-doped $\alpha\text{-Fe}_2\text{O}_3$ is found between 100 and 390 nm, where excited electrons transit directly between the 2p orbitals of the VB and the 3d orbitals of the CB [32, 75]. In the visible spectrum range, the smaller E_g allows for greater sunlight absorption, enhancing photon-electron interactions during the charge carrier transition between the CB and VB, ultimately increasing the absorption coefficient and improving photocatalytic activity.

The calculated value for absorption coefficient for (B, Y) and (B, Nb) co-doped $\alpha\text{-Fe}_2\text{O}_3$ showed significant improvement in the visible spectrum, outperforming pristine $\alpha\text{-Fe}_2\text{O}_3$ across the wavelength range of 100 to 1000 nm, as illustrated in Fig. 6(b). In the ultraviolet (UV) region, (B, Nb) co-doped $\alpha\text{-Fe}_2\text{O}_3$ exhibited the highest rate of photon-electron interactions for charge carrier transitions between the CB and VB, leading to enhanced photoconversion efficiency. Likewise, (B, Y) co-doped $\alpha\text{-Fe}_2\text{O}_3$ displayed higher photoconversion efficiency than pristine $\alpha\text{-Fe}_2\text{O}_3$ due to the enhanced delocalization of charge carriers within the CBM and VBM. In addition, the smaller E_g for both combinations of co-dopants played a crucial role in the value of α at longer wavelengths. Therefore, the results reveal that (B, Y) and (B, Nb) are the most effective co-dopants for doping and enhancing the photocatalytic activity of $\alpha\text{-Fe}_2\text{O}_3$, making it a promising photoelectrode for efficient and sustainable photoelectrochemical water splitting applications.

4 Conclusion

In summary, we focused on enhancing the electronic and optical properties of $\alpha\text{-Fe}_2\text{O}_3$ through mono-doping and co-doping techniques with non-metal elements, B, and metal elements, Y and Nb. By employing the substitutional doping method, we found that the mono-dopants, Y and Nb, and the co-dopants, (B, Y) and (B, Nb), exhibited favorable thermodynamic phase stability and improved material properties. These improvements included a higher D and a preferable μ_ε , enhancing the conductivity and photocatalytic activity. Among the mono-dopants, B-doped $\alpha\text{-Fe}_2\text{O}_3$ demonstrated a reduced E_g . However, it encountered challenges forming impurity bands between the CB and VB. These challenges were addressed by utilizing co-dopants (B, Y) and (B, Nb) that significantly reduced E_g , facilitating light absorption in the visible spectrum. The metal dopants exhibited a higher positive ionic charge, increasing the charge carrier density and J_{ph} . In addition,

the delocalization of charge carriers in CBM and VBM contributed to the efficient charge transport toward the photoelectrode surface, further improving photocatalytic activity. The absorption of solar energy in the visible region generated more excited charge carriers in the d-orbitals, increasing J_{ph} in photocatalytic water splitting. These findings demonstrate that co-doping with the proposed dopants is the most effective strategy for optimizing growth mechanisms and substantially improving the optoelectronic properties and photocatalytic activity of α -Fe₂O₃, showcasing its potential to advance efficient and sustainable photoelectrochemical water splitting in renewable energy applications.

Supplementary material

The supplementary material contains the X-ray diffraction patterns, electronic band structures, and density of states of the pristine and doped α -Fe₂O₃ materials.

Data availability

All data in the paper are present in the main text, which will also be available from the corresponding author upon reasonable request.

Author Declaration

The authors have no conflicts to disclose.

Acknowledgments

The authors gratefully acknowledge financial support from Neural Semiconductor Limited (NSL) and computational support from the Photonics Laboratory, Department of Electrical and Electronic Engineering (EEE), Bangladesh University of Engineering and Technology (BUET).

References

- [1] Y.-H. Chiu, T.-H. Lai, M.-Y. Kuo, P.-Y. Hsieh, and Y.-J. Hsu, "Photoelectrochemical cells for solar hydrogen production: Challenges and opportunities," *APL Materials*, vol. 7, no. 8, 2019.

- [2] J. Jia, L. C. Seitz, J. D. Benck, Y. Huo, Y. Chen, J. W. D. Ng, T. Bilir, J. S. Harris, and T. F. Jaramillo, "Solar water splitting by photovoltaic-electrolysis with a solar-to-hydrogen efficiency over 30%," Nature communications, vol. 7, no. 1, p. 13237, 2016.
- [3] Z. Li, S. Fang, H. Sun, R.-J. Chung, X. Fang, and J.-H. He, "Solar hydrogen," Advanced Energy Materials, vol. 13, no. 8, p. 2203019, 2023.
- [4] Z. Li, W. Luo, M. Zhang, J. Feng, and Z. Zou, "Photoelectrochemical cells for solar hydrogen production: current state of promising photoelectrodes, methods to improve their properties, and outlook," Energy & Environmental Science, vol. 6, no. 2, pp. 347–370, 2013.
- [5] A. Thakur, D. Ghosh, P. Devi, K.-H. Kim, and P. Kumar, "Current progress and challenges in photoelectrode materials for the production of hydrogen," Chemical Engineering Journal, vol. 397, p. 125415, 2020.
- [6] K. Sivula and R. Van De Krol, "Semiconducting materials for photoelectrochemical energy conversion," Nature Reviews Materials, vol. 1, no. 2, pp. 1–16, 2016.
- [7] A. A. Mamun, A. Billah, and M. A. Talukder, "Effects of activation overpotential in photoelectrochemical cells considering electrical and optical configurations," Heliyon, vol. 9, no. 6, 2023.
- [8] J. R. Hemmerling, A. Mathur, and S. Linic, "Design principles for efficient and stable water splitting photoelectrocatalysts," Accounts of Chemical Research, vol. 54, no. 8, pp. 1992–2002, 2021.
- [9] M. G. Walter, E. L. Warren, J. R. McKone, S. W. Boettcher, Q. Mi, E. A. Santori, and N. S. Lewis, "Correction to solar water splitting cells," Chemical Reviews, vol. 111, no. 9, pp. 5815–5815, 2011.
- [10] N. A. R. Che Mohamad, F. Marques Mota, and D. H. Kim, "Photocatalytic and photoelectrochemical overall water splitting," Solar-to-Chemical Conversion: Photocatalytic and Photoelectrochemical Processes, pp. 189–242, 2021.
- [11] F. Qureshi and M. Tahir, "Photoelectrochemical water splitting with engineering aspects for hydrogen production: Recent advances, strategies and challenges," International Journal of Hydrogen Energy, vol. 69, pp. 760–776, 2024.
- [12] A. A. Mamun, A. Billah, and M. A. Talukder, "Enhancing hydrogen evolution reaction using iridium atomic monolayer on conventional electrodes: A first-principles study," International Journal of Hydrogen Energy, vol. 59, pp. 982–990, 2024.
- [13] R. Gao, J. Zhu, and D. Yan, "Transition metal-based layered double hydroxides for photo (electro) chemical water splitting: a mini review," Nanoscale, vol. 13, no. 32, pp. 13593–13603, 2021.
- [14] M. I. Díez-García and R. Gómez, "Progress in ternary metal oxides as photocathodes for water splitting cells: Optimization strategies," Solar RRL, vol. 6, no. 4, p. 2100871, 2022.

- [15] I. Hamdani and A. Bhaskarwar, “Recent progress in material selection and device designs for photoelectrochemical water-splitting,” Renewable and Sustainable Energy Reviews, vol. 138, p. 110503, 2021.
- [16] J. Jian and J. Sun, “A review of recent progress on silicon carbide for photoelectrochemical water splitting,” Solar RRL, vol. 4, no. 7, p. 2000111, 2020.
- [17] T. Higashi, H. Nishiyama, V. Nandal, Y. Pihosh, Y. Kawase, R. Shoji, M. Nakabayashi, Y. Sasaki, N. Shibata, H. Matsuzaki, et al., “Design of semitransparent tantalum nitride photoanode for efficient and durable solar water splitting,” Energy & Environmental Science, vol. 15, no. 11, pp. 4761–4775, 2022.
- [18] H. Lu, X. Li, S. A. Monny, Z. Wang, and L. Wang, “Photoelectrocatalytic hydrogen peroxide production based on transition-metal-oxide semiconductors,” Chinese Journal of Catalysis, vol. 43, no. 5, pp. 1204–1215, 2022.
- [19] I. Barba-Nieto, N. Gomez-Cerezo, A. Kubacka, and M. Fernandez-Garcia, “Oxide-based composites: applications in thermo-photocatalysis,” Catalysis Science & Technology, vol. 11, no. 21, pp. 6904–6930, 2021.
- [20] D. K. Lee, D. Lee, M. A. Lumley, and K.-S. Choi, “Progress on ternary oxide-based photoanodes for use in photoelectrochemical cells for solar water splitting,” Chemical Society Reviews, vol. 48, no. 7, pp. 2126–2157, 2019.
- [21] T. Yao, X. An, H. Han, J. Q. Chen, and C. Li, “Photoelectrocatalytic materials for solar water splitting,” Advanced Energy Materials, vol. 8, no. 21, p. 1800210, 2018.
- [22] J. Wang, T. van Ree, Y. Wu, P. Zhang, and L. Gao, “Metal oxide semiconductors for solar water splitting,” in Metal Oxides in Energy Technologies, pp. 205–249, Elsevier, 2018.
- [23] K. W. Tan, C. M. Yap, Z. Zheng, C. Y. Haw, P. S. Khiew, and W. S. Chiu, “State-of-the-art advances, development, and challenges of metal oxide semiconductor nanomaterials for photothermal solar steam generation,” Advanced Sustainable Systems, vol. 6, no. 4, p. 2100416, 2022.
- [24] L. Yang, F. Li, and Q. Xiang, “Advances and challenges in the modification of photoelectrode materials for photoelectrocatalysis water splitting,” Materials Horizons, 2024.
- [25] M. G. Mali, S. An, M. Liou, S. S. Al-Deyab, and S. S. Yoon, “Photoelectrochemical solar water splitting using electrospun TiO₂ nanofibers,” Applied Surface Science, vol. 328, pp. 109–114, 2015.
- [26] C. Zhou, Z. Sanders-Bellis, T. J. Smart, W. Zhang, L. Zhang, Y. Ping, and M. Liu, “Interstitial lithium doping in BiVO₄ thin film photoanode for enhanced solar water splitting activity,” Chemistry of Materials, vol. 32, no. 15, pp. 6401–6409, 2020.

- [27] T. Singh, R. Müller, J. Singh, and S. Mathur, "Tailoring surface states in WO₃ photoanodes for efficient photoelectrochemical water splitting," Applied Surface Science, vol. 347, pp. 448–453, 2015.
- [28] Z. Najaf, D. L. T. Nguyen, S. Y. Chae, O.-S. Joo, A. U. H. A. Shah, D.-V. N. Vo, V.-H. Nguyen, Q. Van Le, and G. Rahman, "Recent trends in development of hematite (α -Fe₂O₃) as an efficient photoanode for enhancement of photoelectrochemical hydrogen production by solar water splitting," International Journal of Hydrogen Energy, vol. 46, no. 45, pp. 23334–23357, 2021.
- [29] A. Kay, I. Cesar, and M. Grätzel, "New benchmark for water photooxidation by nanostructured α -Fe₂O₃ films," Journal of the American Chemical Society, vol. 128, no. 49, pp. 15714–15721, 2006.
- [30] A. B. Murphy, P. R. Barnes, L. K. Randeniya, I. C. Plumb, I. E. Grey, M. D. Horne, and J. A. Glasscock, "Efficiency of solar water splitting using semiconductor electrodes," International journal of hydrogen energy, vol. 31, no. 14, pp. 1999–2017, 2006.
- [31] R. Franking, L. Li, M. A. Lukowski, F. Meng, Y. Tan, R. J. Hamers, and S. Jin, "Facile post-growth doping of nanostructured hematite photoanodes for enhanced photoelectrochemical water oxidation," Energy & Environmental Science, vol. 6, no. 2, pp. 500–512, 2013.
- [32] R. Gardner, F. Sweett, and D. Tanner, "The electrical properties of alpha ferric oxide-II.: Ferric oxide of high purity," Journal of Physics and Chemistry of Solids, vol. 24, no. 10, pp. 1183–1196, 1963.
- [33] I. Balberg and H. Pinch, "The optical absorption of iron oxides," Journal of magnetism and magnetic materials, vol. 7, no. 1-4, pp. 12–15, 1978.
- [34] A. G. Tamirat, J. Rick, A. A. Dubale, W.-N. Su, and B.-J. Hwang, "Using hematite for photoelectrochemical water splitting: a review of current progress and challenges," Nanoscale horizons, vol. 1, no. 4, pp. 243–267, 2016.
- [35] A. Ali, F. Long, and P. K. Shen, "Innovative strategies for overall water splitting using nanostructured transition metal electrocatalysts," Electrochemical Energy Reviews, vol. 5, no. 4, p. 1, 2022.
- [36] A. Tofanello, S. Shen, F. L. de Souza, and L. Vayssieres, "Strategies to improve the photoelectrochemical performance of hematite nanorod-based photoanodes," APL Materials, vol. 8, no. 4, 2020.
- [37] J. Park, J. Kang, S. Chaule, and J.-H. Jang, "Recent progress and perspectives on heteroatom doping of hematite photoanodes for photoelectrochemical water splitting," Journal of Materials Chemistry A, 2023.
- [38] Y. Ling, G. Wang, D. A. Wheeler, J. Z. Zhang, and Y. Li, "Sn-doped hematite nanostructures for photoelectrochemical water splitting," Nano Letters, vol. 11, no. 5, pp. 2119–2125, 2011.
- [39] J. Y. Kim, G. Magesh, D. H. Youn, J.-W. Jang, J. Kubota, K. Domen, and J. S. Lee, "Single-crystalline, wormlike hematite photoanodes for efficient solar water splitting," Scientific Reports, vol. 3, no. 1, p. 2681, 2013.

- [40] S. Shen, J. Jiang, P. Guo, C. X. Kronawitter, S. S. Mao, and L. Guo, "Effect of Cr doping on the photoelectrochemical performance of hematite nanorod photoanodes," Nano Energy, vol. 1, no. 5, pp. 732–741, 2012.
- [41] L. Wang, C.-Y. Lee, and P. Schmuki, "Ti and Sn co-doped anodic α -Fe₂O₃ films for efficient water splitting," Electrochemistry communications, vol. 30, pp. 21–25, 2013.
- [42] T. Morikawa, T. Arai, and T. Motohiro, "Photoactivity of p-type α -Fe₂O₃ induced by anionic/cationic codoping of N and Zn," Applied physics express, vol. 6, no. 4, p. 041201, 2013.
- [43] A. Annamalai, H. H. Lee, S. H. Choi, S. Y. Lee, E. Gracia-Espino, A. Subramanian, J. Park, K.-J. Kong, and J. S. Jang, "Sn/Be sequentially co-doped hematite photoanodes for enhanced photoelectrochemical water oxidation: effect of Be²⁺ as co-dopant," Scientific Reports, vol. 6, no. 1, p. 23183, 2016.
- [44] C. Herfeld and M. Ivanova, "Introduction: first principles in sciencetheir status and justification," Synthese, vol. 198, pp. 3297–3308, 2021.
- [45] H. Pan, X. Meng, D. Liu, S. Li, and G. Qin, "(Ti/Zr, N) codoped hematite for enhancing the photoelectrochemical activity of water splitting," Physical Chemistry Chemical Physics, vol. 17, no. 34, pp. 22179–22186, 2015.
- [46] X. Kong, H. Zhang, Y. Xiao, C. Cao, Y. Shi, and G. Pang, "Effective, transition metal free and selective C–F activation under mild conditions," RSC Advances, vol. 5, no. 10, pp. 7035–7048, 2015.
- [47] A. Kleiman-Shwarsctein, M. N. Huda, A. Walsh, Y. Yan, G. D. Stucky, Y.-S. Hu, M. M. Al-Jassim, and E. W. McFarland, "Electrodeposited aluminum-doped α -Fe₂O₃ photoelectrodes: experiment and theory," Chemistry of Materials, vol. 22, no. 2, pp. 510–517, 2010.
- [48] M. Wu, H. Zhu, J. Wang, J. Wang, and J. Zhu, "Hydrogen diffusion in Ni-doped iron structure: A first-principles study," Chemical Physics Letters, vol. 831, p. 140844, 2023.
- [49] P. Giannozzi, S. Baroni, N. Bonini, M. Calandra, R. Car, C. Cavazzoni, D. Ceresoli, G. L. Chiarotti, M. Cococcioni, I. Dabo, et al., "Quantum espresso: a modular and open-source software project for quantum simulations of materials," Journal of physics: Condensed matter, vol. 21, no. 39, p. 395502, 2009.
- [50] P. Giannozzi, O. Andreussi, T. Brumme, O. Bunau, M. B. Nardelli, M. Calandra, R. Car, C. Cavazzoni, D. Ceresoli, M. Cococcioni, et al., "Advanced capabilities for materials modelling with quantum espresso," Journal of physics: Condensed matter, vol. 29, no. 46, p. 465901, 2017.
- [51] G. Kresse and D. Joubert, "From ultrasoft pseudopotentials to the projector augmented-wave method," Physical Review B, vol. 59, no. 3, p. 1758, 1999.
- [52] H. J. Monkhorst and J. D. Pack, "Special points for Brillouin-zone integrations," Physical Review B, vol. 13, no. 12, p. 5188, 1976.

- [53] S. L. Dudarev, G. A. Botton, S. Y. Savrasov, C. Humphreys, and A. P. Sutton, "Electron-energy-loss spectra and the structural stability of nickel oxide: An LSDA+U study," Physical Review B, vol. 57, no. 3, p. 1505, 1998.
- [54] N. J. Mosey, P. Liao, and E. A. Carter, "Rotationally invariant ab initio evaluation of Coulomb and exchange parameters for DFT+U calculations," The Journal of Chemical Physics, vol. 129, no. 1, 2008.
- [55] T. T. Smith, "The magnetic properties of hematite," Physical Review, vol. 8, no. 6, p. 721, 1916.
- [56] M. Tadic, M. Panjan, Y. Lalatone, I. Milosevic, B. V. Tadic, and J. Lazovic, "Magnetic properties, phase evolution, hollow structure and biomedical application of hematite (α -Fe₂O₃) and QUAIPH," Advanced Powder Technology, vol. 33, no. 12, p. 103847, 2022.
- [57] F. Morin, "Magnetic susceptibility of α -Fe₂O₃ and α -Fe₂O₃ with added titanium," Physical Review, vol. 78, no. 6, p. 819, 1950.
- [58] J. Wang, H. Sun, J. Huang, Q. Li, and J. Yang, "Band structure tuning of TiO₂ for enhanced photoelectrochemical water splitting," The Journal of Physical Chemistry C, vol. 118, no. 14, pp. 7451–7457, 2014.
- [59] F. Kraushofer, Z. Jakub, M. Bichler, J. Hulva, P. Drmota, M. Weinold, M. Schmid, M. Setvin, U. Diebold, P. Blaha, et al., "Atomic-scale structure of the hematite α -Fe₂O₃ (1102)R-Cut Surface," The Journal of Physical Chemistry C, vol. 122, no. 3, pp. 1657–1669, 2018.
- [60] G. Williamson and W. Hall, "X-ray line broadening from filed aluminium and wolfram," Acta Metallurgica, vol. 1, no. 1, pp. 22–31, 1953.
- [61] K. Momma and F. Izumi, "Vesta: a three-dimensional visualization system for electronic and structural analysis," Journal of Applied Crystallography, vol. 41, no. 3, pp. 653–658, 2008.
- [62] B. Modak, K. Srinivasu, and S. K. Ghosh, "Band gap engineering of NaTaO₃ using density functional theory: a charge compensated codoping strategy," Physical Chemistry Chemical Physics, vol. 16, no. 32, pp. 17116–17124, 2014.
- [63] L. Pauling and S. B. Hendricks, "The crystal structures of hematite and corundum," Journal of the American Chemical Society, vol. 47, no. 3, pp. 781–790, 1925.
- [64] L. W. Finger and R. M. Hazen, "Crystal structure and isothermal compression of Fe₂O₃, Cr₂O₃, and V₂O₃ to 50 kbars," Journal of Applied Physics, vol. 51, no. 10, pp. 5362–5367, 1980.
- [65] Y. Meng, X.-W. Liu, C.-F. Huo, W.-P. Guo, D.-B. Cao, Q. Peng, A. Dearden, X. Gonze, Y. Yang, J. Wang, et al., "When density functional approximations meet iron oxides," Journal of Chemical Theory and Computation, vol. 12, no. 10, pp. 5132–5144, 2016.

- [66] L. Pun, G. C. Soares, M. Isakov, and M. Hokka, "Effects of strain rate on strain-induced martensite nucleation and growth in 301LN metastable austenitic steel," Materials Science and Engineering: A, vol. 831, p. 142218, 2022.
- [67] V. Dhanasekaran, T. Mahalingam, and R. Chandramohan, "Post heat treatment effect on electrochemically synthesized CuO thin films," ECS Transactions, vol. 45, no. 24, p. 73, 2013.
- [68] M. Tahir, M. Fakhar-e Alam, M. Atif, G. Mustafa, and Z. Ali, "Investigation of optical, electrical and magnetic properties of hematite α -Fe₂O₃ nanoparticles via sol-gel and co-precipitation method," Journal of King Saud University-Science, vol. 35, no. 5, p. 102695, 2023.
- [69] U. Utari, R. Arilasita, S. Suharno, H. Widiyandari, and B. Purnama, "Effect of synthesis temperature on structural and magnetic properties in hematite (α -Fe₂O₃) nanoparticles produced by co-precipitation method," in Defect and Diffusion Forum, vol. 417, pp. 219–225, Trans Tech Publ, 2022.
- [70] M. J. Iqbal, N. Yaqub, B. Sepiol, and B. Ismail, "A study of the influence of crystallite size on the electrical and magnetic properties of CuFe₂O₄," Materials Research Bulletin, vol. 46, no. 11, pp. 1837–1842, 2011.
- [71] M. Rincón Joya, J. Barba Ortega, J. O. D. Malafatti, and E. C. Paris, "Evaluation of photocatalytic activity in water pollutants and cytotoxic response of α -Fe₂O₃ nanoparticles," ACS Omega, vol. 4, no. 17, pp. 17477–17486, 2019.
- [72] J. Oh, H. Ryu, and W.-J. Lee, "Effects of Fe doping on the photoelectrochemical properties of CuO photoelectrodes," Composites Part B: Engineering, vol. 163, pp. 59–66, 2019.
- [73] T. Bak, J. Nowotny, M. Rekas, and C. Sorrell, "Photo-electrochemical hydrogen generation from water using solar energy. materials-related aspects," International journal of hydrogen energy, vol. 27, no. 10, pp. 991–1022, 2002.
- [74] K. Sivula, F. Le Formal, and M. Grätzel, "Solar water splitting: progress using hematite (α -Fe₂O₃) photoelectrodes," ChemSusChem, vol. 4, no. 4, pp. 432–449, 2011.
- [75] J. L. Shelton and K. E. Knowles, "Polaronic optical transitions in hematite (α -Fe₂O₃) revealed by first-principles electron–phonon coupling," The Journal of Chemical Physics, vol. 157, no. 17, 2022.